Radiation Physics and Chemistry 168 (2020) 108572

Contents lists available at ScienceDirect

Radiation Physics and Chemistry

journal homepage: www.elsevier.com/locate/radphyschem

Evaluation of the dose distribution of tomotherapy using polymer gel dosimeters and optical computed tomography with ring artifact correction

Ying-Hsiang Chou[a,b], Yu-Chan Lu[b], Shin-Lei Peng[c], Shan-Chih Lee[a,d], Ling-Ling Hsieh[e,**,1], Cheng-Ting Shih[a,d,*,1]

[a] Department of Medical Imaging and Radiological Sciences, Chung Shan Medical University, 40201, Taichung, Taiwan
[b] Department of Radiation Oncology, Chung Shan Medical University Hospital, 40201, Taichung, Taiwan
[c] Department of Biomedical Imaging and Radiological Science, College of Health Care, China Medical University, 40402, Taichung, Taiwan
[d] Department of Medical Imaging, Chung Shan Medical University Hospital, 40201, Taichung, Taiwan
[e] Department of Medical Imaging and Radiological Sciences, Central Taiwan University of Science and Technology, 40601, Taichung, Taiwan

ARTICLE INFO

Keywords:
Helical tomotherapy
Polymer gel dosimeter
Optical computed tomography
Ring artifact correction
Gamma evaluation

ABSTRACT

Helical tomotherapy (HT) can provide highly conformal dose distribution through multiple-beam irradiation. Evaluation of such dose distribution is essential to ensure the quality of radiotherapy. In this study, we evaluated the performance of measuring the 3D dose distribution delivered by the HT using an *N*-Isopropylacrylamide (NIPAM) polymer gel dosimeter (PGD) and optical computed tomography (CT) with ring artifact correction. The 3D dose distribution of a real clinical case of cerebral arteriovenous malformation was measured using the NIPAM PGD. The irradiated PGD was scanned using an optical CT scanner 24-hr after dose delivery. The ring artifact correction was performed by median filtering of the acquired optical CT images in polar coordinates. The optical CT images without and with ring artifact correction were compared. The converted dose distributions from the optical CT images were compared with those generated from a treatment planning system using a gamma evaluation. Results show that the NIPAM PGD could accurately record the dose distribution delivered by the tomography. Also, ring artifact correction with proper filter length could effectively reduce the artifacts and improve the uniformity of the measured dose distribution. The pass rate of the measured dose distribution calculated using a three-dimensional gamma evaluation with 3%/3 mm criteria from 89.2% to 99.7% after ring artifact correction. We concluded that the NIPAM PGD and optical CT with ring artifact correction could be useful for pre-treatment verification of the HT.

1. Introduction

In clinical radiotherapy, radiation exposure of critical organs and noncancerous tissues is expected to be minimized to reduce the damage on healthy or critical organs and tissues. Dose delivery techniques with high precision and high dose gradient can facilitate high-quality radiation therapy by enhancing the tumor control probability while reducing the normal tissues complication probability (Fiorino et al., 2006). Helical tomotherapy (HT) is thereby proposed to provide high precision radiotherapy. In the HT, a ring gantry of rotating exposure mechanism similar to that used in computed tomography (CT) scanners is applied to emit multiangle intensity-modulated fan beams with high conformity (Welsh et al., 2002; Lee et al., 2008). Additionally, the HT can be integrated with CT images to perform image-guided radiation therapy. By correcting the treatment plan before every treatment session to account the motion errors caused by patients' postures (Forrest et al., 2004; Ramsey et al., 2006), irradiation precision comparable to that obtained using the X-knife or the Cyberknife systems can be achieved (Stiebel-Kalish et al., 2012; Krause et al., 2013). Moreover, the HT can also be used in large-scale radiation therapy to avoid the limits of conventional intensity-modulated radiation therapy which must be performed in multiple sections for a large irradiation area. The HT facilitates a full dose delivered in a single exposure; this greatly reduces the complexity of the irradiation process (Rochet et al., 2008; Wong et al., 2009).

To ensure that the dose delivery to patients through the HT

* Corresponding author. Department of Medical Imaging and Radiological Sciences, Chung Shan Medical University, 40201, Taichung, Taiwan.
** Corresponding author.
E-mail addresses: llhsieh@ctust.edu.tw (L.-L. Hsieh), ctshih21@gmail.com (C.-T. Shih).
[1] Cheng-Ting Shih and Ling-Ling Hsieh contributed equally to this work.

https://doi.org/10.1016/j.radphyschem.2019.108572
Received 30 July 2019; Received in revised form 3 November 2019; Accepted 7 November 2019
Available online 08 November 2019
0969-806X/

technique is matched to the treatment plan, performing dose verification before and after treatment administration is crucial. Several studies have been comprehensively confirmed that the accuracy and efficacy of polymer gel dosimeters (PGDs) on the verification of 3D dose distribution (Chen et al., 2014; Hsieh et al., 2017). The PGD is not influenced by the ion diffusion effect, which is an inherent problem for the Fricke gel dosimeters (Maryanski et al., 1993); therefore, the PGDs can accurately record and reflect highly complex dose distribution features. Currently, a variety of the PGDs with different formulas have been proposed and applied in the measurement of radiation dose. After the predetermined dose distribution is delivered, the PGD undergo changes in their physical properties through polymerized and crosslinked reactions (Shih et al., 2013). The extent of its reactions is proportionate to the dose received. The dose distribution recorded by the PGD can then be interpreted using several imaging devices, including magnetic resonance imaging (Hsieh et al., 2017), CT (Johnston et al., 2015), and optical CT (optical CT) (Shih et al., 2015). Among these techniques, the optical CT possesses advantages such as high spatial resolution, rapid imaging, and cost-effectiveness. More importantly, the optical CT does not cause secondary exposure, which is an inherent problem of the readout of the PGD using CT (Baxter et al., 2007).

The optical CT uses lasers to perform PGD scanning. The polymer structures that form after the radiation-induced polymerization of PGDs cause the attenuation or scattering of photons, thus reducing the light transmissivity of PDGs (Shih et al., 2015). When photosensitive elements, such as charge-coupled devices or complementary metal-oxide semiconductors, are used to measure the intensity of lasers penetrating PGDs, different light transmissivities can be detected through the different paths used by PGDs to receive different doses. After sinograms are obtained through a series of multiangle projection scans, the optical CT images that reflect the dose distribution can be generated using image reconstruction techniques. However, the photosensitive elements used in the laser measurement might provide unstable responses, resulted in inconsistent projection information. Eventually, ring artifacts present in the reconstructed images. These artifacts form erroneous dose features and greatly reduce the effectiveness of the optical CT in the readout of the PGD (Oldham and Kim, 2004).

In this study, the performance of a low-toxicity *N*-isopropyl-acrylamide (NIPAM) PGD on measuring the distribution of radiation doses delivered by the HT for the treatment of cerebral arteriovenous malformation was evaluated. The dose readout of the irradiated NIPAM PGD was conducted using an optical CT scanner, and the acquired dose distribution was compared with the reference distribution outputted from a treatment planning system (TPS). In addition, ring artifact correction was performed to improve the quality of acquired optical CT images and converted dose distributions. The results indicated that the NIPAM PGD could accurately measure the distribution of doses delivered by the HT, and ring artifact correction could further improve the measured dose distribution. We thought that the NIPAM PGDs and the optical CT with ring artifact correction can be used in the pre- and post-treatment dose verification of the HT in clinical.

2. Materials and methods

2.1. NIPAM gel preparation

The NIPAM PGDs used in this study were prepared using a formula modified on the basis of the formula developed by Senden et al. (2006). The composition of the NIPAM PGDs used in this study and detailed weight percentages are as follows: 5% NIPAM monomer (97%, Sigma-Aldrich, St. Louis, MO, USA), 5% gelatin (300 Bloom Tape A, Sigma-Aldrich, St. Louis, MO, USA), 3% crosslinking agent *N*,*N*′-methylene-bis-acrylamide (BIS, Merck, Darmstadt, Germany), 10% antioxidant agent tetrakis (hydroxymethyl) phosphonium chloride (THPC) (80%, Sigma-Aldrich, St. Louis, MO, USA), and 89% deionized water (Hsieh et al., 2017). The production process of the NIPAM PGDs is as follows:

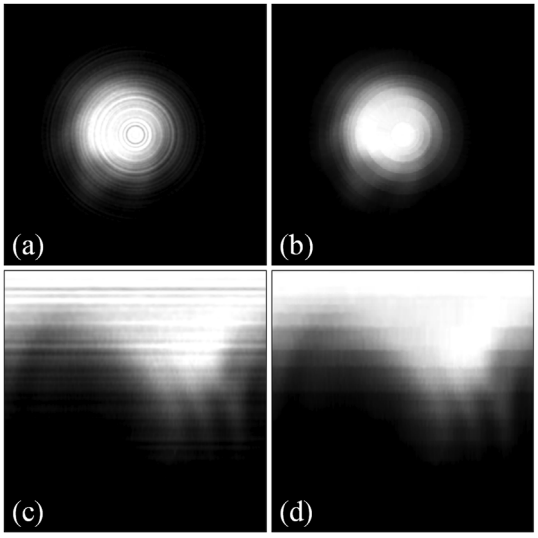

Fig. 1. (a) An original optical CT image acquired at the center of the dose volume from the gel phantom. (b) The ring artifact-corrected images of (a) using a 55-pixel median filter. (c) and (d) are the polar transformation results of (a) and (b), respectively.

first, deionized water with gelatin at a temperature less than 22 °C was mixed and stirred for 10 min. Next, the gelatin-water solution was heated at 45 °C until the solution turned clear. Then, THPC was immediately added to the solution. The mixture was then stirred for 15 min. Next, the prepared gels were placed into calibration tubes for dose calibration and into a cylindrical gel phantom for the measurement of the output dose distribution. The calibration tubes and cylindrical gel phantom were sealed with Parafilm, covered with aluminum foil, and stored in a refrigerator at a temperature of 4 °C for 6 h to prevent light- or heat-induced polymerization before the gels had completely hardened. Additionally, after irradiation and before optical CT scanning, both the calibration tubes and the gel phantom were placed in a clinical examination room at room temperature (i.e., approximately 22 °C) to avoid the occurrence of heat-induced polymerization.

2.2. Dose delivery

The dose delivery of the calibration tubes and gel phantom was performed using a HT device (TomoTherapy Hi-Art system, TomoTherapy Incorporated, WI, USA); The HT device exhibited an output error lower than 2% in the daily quality assurance checks. Absorbed doses of 0, 1, 2, 5, 8, and 12 Gy were delivered to the calibration tubes to establish the dose-response curve of the NIPAM PGDs. The irradiation parameters were as follows: photon beam energy = 6 MV, source-to-axis distance = 85 cm, dose rate = 662 cGy/min, and emittance angle = 0°. The gel phantom was used to measure the distribution of radiation dose delivered by HT for the treatment of a cerebral arteriovenous malformation case. The irradiation parameters were as follows: photon beam energy = 6 MV, source-to-axis distance = 85 cm, dose rate = 662 cGy/min, prescribed dose at the target region = 10 Gy. The dose distribution in the gel phantom was calculated using the treatment planning system (TPS) (Hi-Art Version 5.1.1, Accuray Operator Station, Accuray, CA, USA), and the result was used as the reference standard for dose distribution. Additionally, a cylindrical phantom with identical geometry to the gel phantom was employed to prevent absorbing radiation of the gel phantom while acquiring CT images for the planning. The cylindrical phantom was filled with gelatin to simulate the photon-attenuation property of the NIPAM PGDs. Scanning of the cylindrical phantom was performed using a CT simulator (Big bore CT, Philips Medical Systems Inc., OH, USA) with the

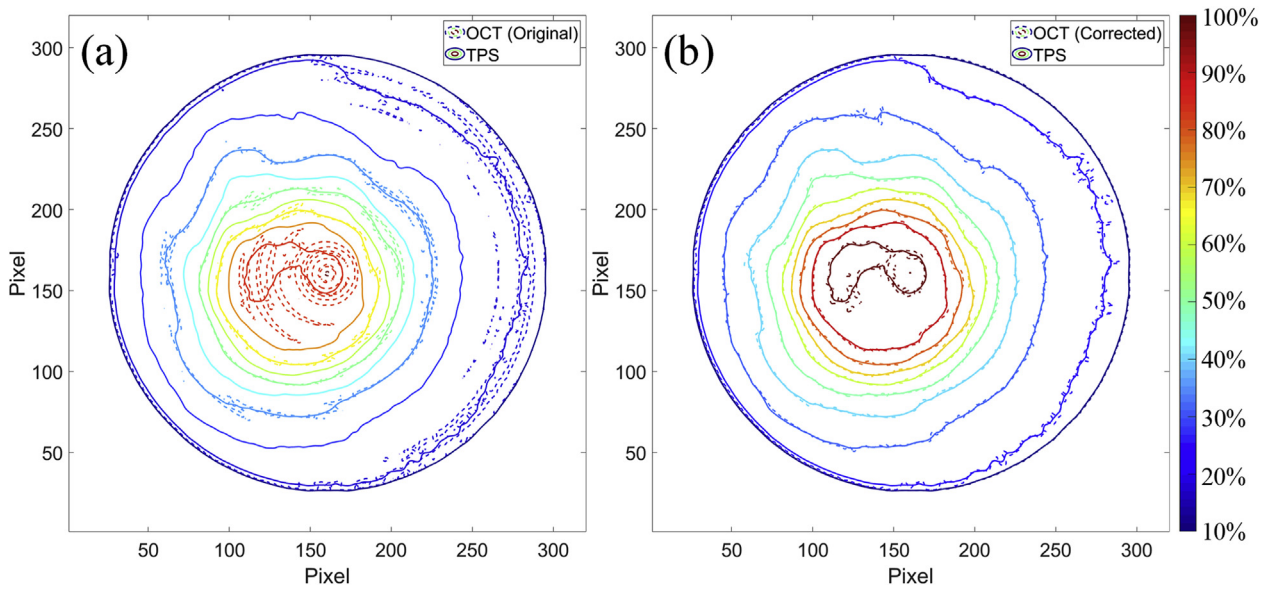

Fig. 2. Isodose curves derived from the dose maps (a) without and (b) with ring artifact correction. The isodose curve derived from the dose map of the TPS is addressed for reference.

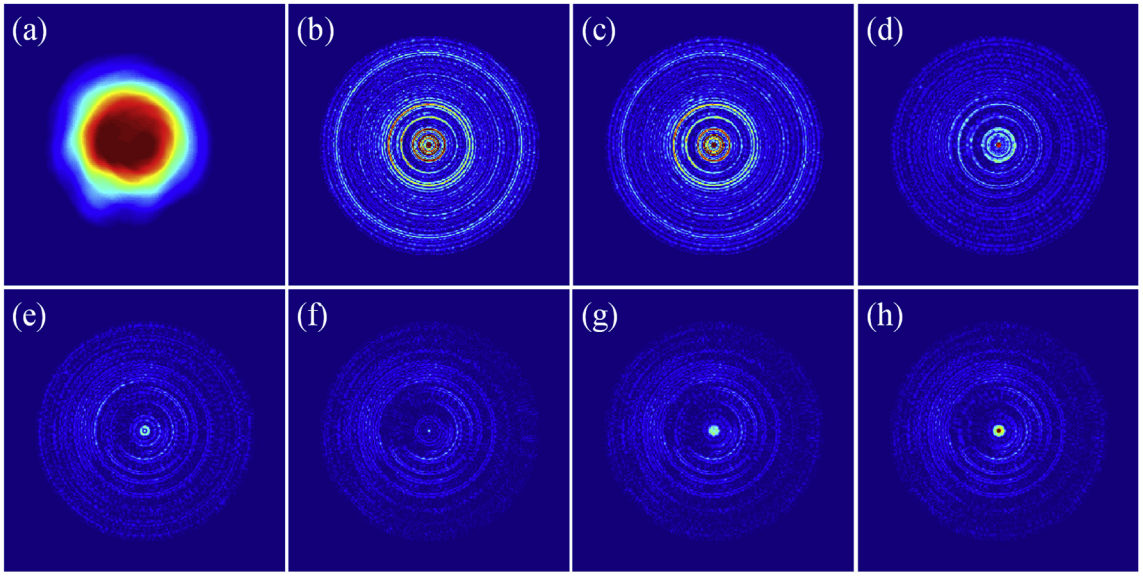

Fig. 3. (a) Dose map at the center of the dose volume outputted from the TPS. (b) The absolute difference maps between the dose maps from the TPS and that converted from Fig. 1 (a). (c)–(h) The absolute difference maps between the dose maps from the TPS and those converted from the ring artifact-corrected images by median filtering with filter lengths of 7, 23, 39, 55, 71, and 87 pixels, respectively.

following parameters: tube voltage of 120 kVp, pitch of 0.563, and slice thickness of 1 mm. The dose delivery of the calibration tubes and gel phantom were performed separately by 30 min to ensure that the dose readout was performed after the same amount of time had elapsed since irradiation.

2.3. Dose readout

In this study, the dose readout was performed using an cone beam-geometric optical CT scanner (DeskCAT, Modus Medical Devices Inc., Ontario, Canada). During scanning, the gel phantom was fixed in the scanning tank, which contained matching liquids that approximated the refractive index of the NIPAM PGDs. Lights with wavelengths of 625 nm emitted by light-emitting diodes were used as the scanning light source, and a complementary metal oxide semiconductor video camera was used to receive the projection. Finally, the optical CT images were reconstructed using the built-in image reconstruction program with a voxel size of $0.25 \times 0.25 \times 0.25\,\mathrm{mm}^3$.

2.4. Ring artifact correction

Ring artifact correction of the optical CT images was conducted using median filtering in the polar coordinate based on the ring artifacts present as streak lines in the polar coordinate and higher image data continuity alone the radial direction in the polar coordinate than in the Cartesian coordinate (Prell et al., 2009). In this study, ring artifact correction was performed in a slice-by-slice manner. The acquired optical CT images were transformed into polar coordinates using the following formula:

$$r = \sqrt{x^2 + y^2} \text{ and } \theta = \arctan\frac{y}{x}, \quad (1)$$

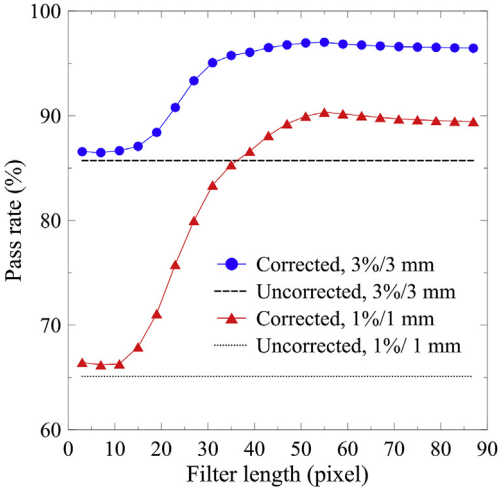

Fig. 4. Pass rates calculated with the 3%/3 mm and 1%/1 mm criteria of the measured dose maps without and with ring artifact correction as a function of the applied length of the median filter.

where x and y represent the spatial coordinates of a pixel in the Cartesian coordinate system, and r and θ represent the corresponding spatial coordinates in the polar coordinate system. In this study, the sampled polar coordinate transformation angle and radial direction were 0.5° and 0.1 mm, respectively. The originally ring-shaped artifacts in the Cartesian coordinate system appeared as streak artifacts along the θ direction in the polar coordinate system. Therefore, performing median filtering along the radial direction can effectively eliminate the ring artifacts. Finally, the corrected images were obtained by performing inverse polar transformation. In addition, the influence of the length of the median filter was evaluated. The results of ring artifact correction using the median filtering with filter lengths from 3 to 87 pixels with a step size of 4 pixels were compared using isodose curve and a gamma evaluation.

2.5. Gamma evaluation

The dose distribution maps were obtained by converting the optical CT images acquired from the irradiated NIPAM PGDs with the dose-response curve. The converted dose distribution map and volume without and with ring artifact correction were compared with the reference dose distribution from the TPS using the 2D and 3D gamma evaluation. Generally, a gamma function that compares the measured dose volume, M, and the reference dose volume, R, is defined as follows:

$$\Gamma(r_m, r_c) = \sqrt{\frac{r^2(r_m, r_c)}{\Delta d^2} + \frac{\delta^2(r_m, r_c)}{\Delta D^2}}, \quad (2)$$

where r_m and r_c represent the spatial coordinates of dose voxels m and c in the measured dose volume M and the reference dose volume R, respectively. The spatial distance between the two dose voxels, r, is defined as $r(r_m,r_c) = |r_m - r_c|$; the dose difference between the two voxels is defined as $\delta(r_m,r_c) = D_m(r_m) - D_c(r_c)$, in which D_m and D_c represent the dose values of voxels m and r, respectively; Δd and ΔD represent the distance-to-agreement (DTA) and dose-difference criterion (DDC), respectively. The γ index of dose voxel m represents the smallest γ value in the spatial volume V; in this study, spatial volume V is defined as a sphere volume with a diameter of 1 cm and the center at dose voxel c (Wendling et al., 2007). The γ index of a voxel smaller than 1 indicates the voxel passed the evaluation. The pass rate was calculated by dividing the number of passed dose voxels by the number of the total dose voxels of the dose volume. In this study, DDC/DTA criteria of 3%/3 mm and 1%/1 mm were applied for the gamma evaluation.

3. Results and discussions

Fig. 1 (a) shows the original optical CT image acquired at the center of the dose volume from the gel phantom. The dose distribution presented in the image is accompanied by obvious ring artifacts. Fig. 1 (c) presents the result of the polar transformation of Fig. 1 (a). The ring artifacts present as horizontal streaks along the azimuthal angle axis in polar coordinates. Fig. 1 (d) illustrates the image obtained by filtering along the radial axis of Fig. 1 (c) using the median filter with a length of 55 pixels. The horizontal streak artifacts were effectively reduced after filtering. Fig. 1 (b) presents the result of the inverse polar transformation of Fig. 1 (d). The median filtering along the radial axis in polar coordinates effectively reduced the ring artifacts. The smoothness of the dose distribution and the continuity of the dose change from the center of the gel phantom outward were improved.

Fig. 2 (a) and (b) present the isodose curves derived from the dose distribution maps converted from Fig. 1 (a) and (b) as well as that outputted from the TPS. The fluctuations induced from the ring artifacts can clearly be observed to manifest in discontinuities and incorrect dose features on the isodose curves. Numerous erroneous dose gradients appear, particularly in the > 80% dose region. By contrast, incorrect isodose curves were effectively eliminated after the artifact correction. The isodose curves derived from the corrected dose map are closed to that outputted from the TPS.

Fig. 3 (a) illustrates the dose distribution outputted from the TPS and Fig. 3 (b) presents the absolute difference map between the dose distribution converted from the original optical CT image and Fig. 3 (a). It can be observed that the differences were mainly caused by the ring

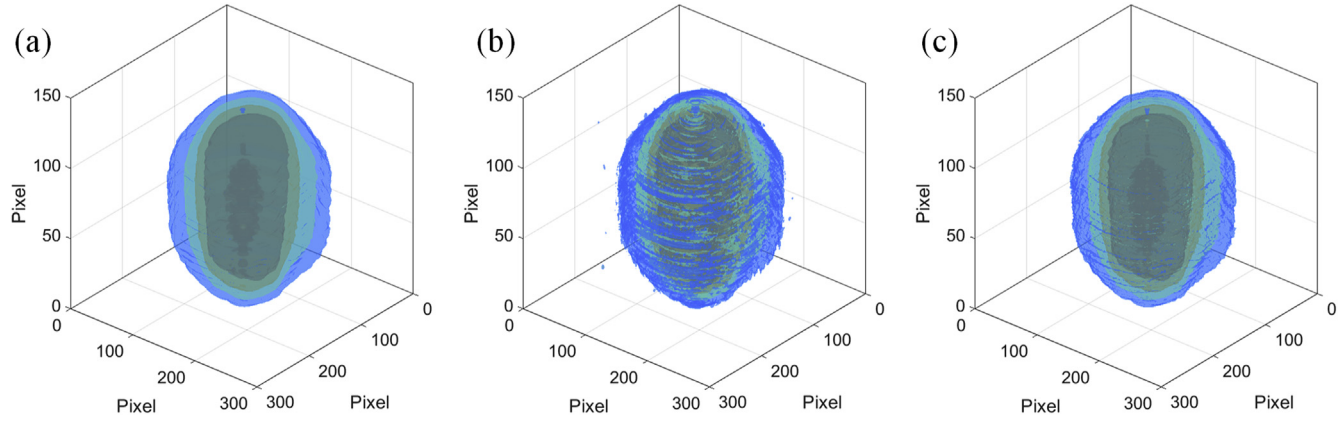

Fig. 5. Isodose surfaces derived from the dose volumes of (a) TPS and the those converted from the optical CT image volume (b) without and (c) with ring artifact correction.

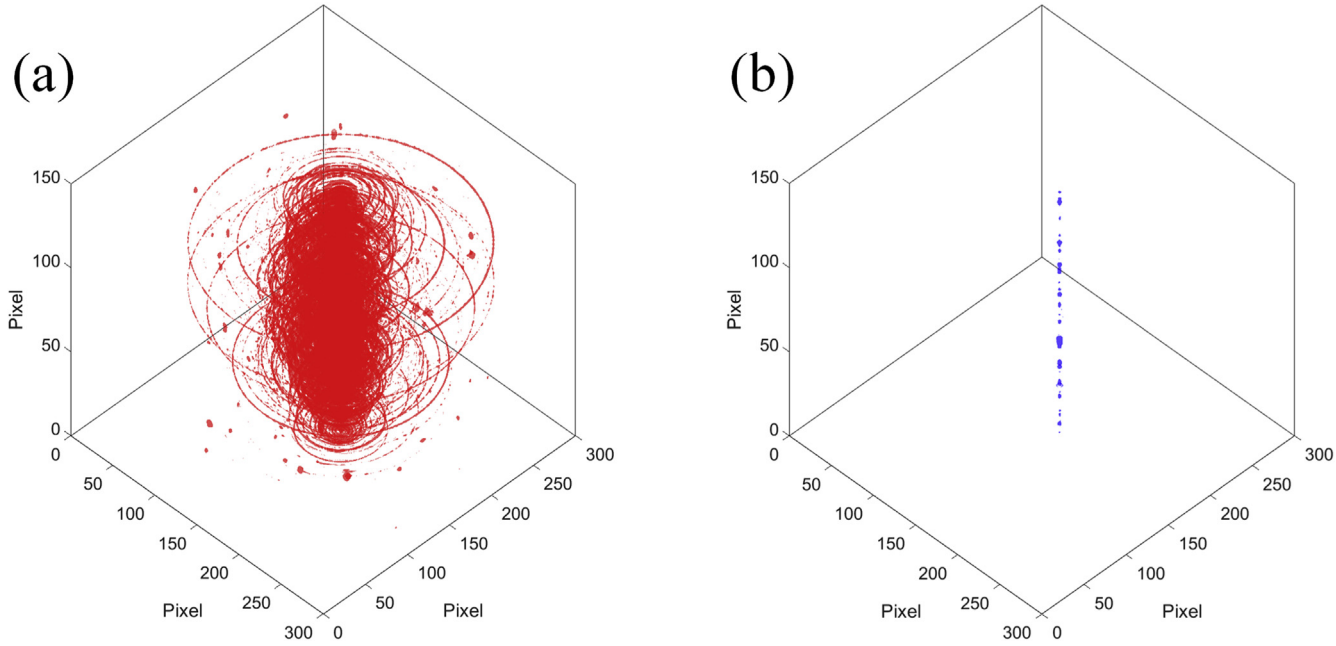

Fig. 6. Voxels that failed the 3D Gamma evaluation with the 3%/3 mm criteria in the dose volumes shown in Fig. 5 (b) and (c).

artifacts and no dose features can be found in the absolute difference map. The pass rate of the 2D gamma evaluation of the dose distribution from the original optical CT image was 85.7%. Fig. 3 (c)–(h) present the absolute difference maps between the dose distribution map from the TPS and those converted from the filtered optimal CT images with filter lengths of 7, 23, 39, 55, 71, and 87 pixels, respectively. Fig. 4 reveals the pass rate as a function of the length of the median filter. The pass rate increased as the filter length increased until the pass rates reached its peak values of 97% with the 3%/3 mm criteria and 90% with the 1%/1 mm criteria at the filter length of 55 pixels. When the filter length longer than 55 pixels, the pass rate decreased as the filter length increased.

As shown in Fig. 3, when the appropriate filter length was applied to perform median filtering, the ring artifacts in the optical CT images could be effectively reduced and the corresponding dose distribution maps became comparable to that from the TPS.

However, over-length filters led to the occurrence of secondary artifacts and consequently an increase in absolute dose differences in the center of the dose distribution, as shown in Fig. 3 (g) and (h). Nevertheless, the pass rates revealed that over-length filters only caused a few incorrect dose features and still could effectively improve the acquired dose distribution compared with that without correction. The severity of ring artifacts may differ among optical CT systems. An appropriate filter length should be selected through pretesting to ensure the correction without inducing secondary artifacts. For the optical CT scanner used in this study, conducting median filtering with a 55 pixel-length filter yielded the optimal pass rate and minimize the influence of ring artifacts.

Fig. 5 present the isodose surfaces derived from the dose volumes of the TPS and the those converted from the optical CT image volume without and with ring artifact correction. Before ring artifact correction was performed, the isodose surfaces appeared to be disorder and showed discontinuity along the *z*-axis. By contrast, the isodose surfaces obtained after ring artifact correction was highly consistent with those of the TPS, indicated that the correction of the ring artifacts can also enhance the continuity and smoothness of doses along the *z*-axis.

Fig. 6 presents the voxels that failed the 3D Gamma evaluation in Fig. 5 (b) and (c). Fig. 6 (a) reveals that the patterns of these points are highly consistent with those of the ring artifacts, indicating the considerable influence of ring artifacts on dose readout. After ring artifact correction, the pass rate was improved from 89.2% to 99.7% with the 3%/3 mm criteria and 61.8%–94.6% with the 1%/1 mm criteria. As shown in Fig. 6 (b), a few points close to the center of the dose volume failed to pass the 3D gamma evaluation after the correction, which is mainly caused by the intrinsic property of the polar transformation. The pixels closed to the center of the optical CT images appeared on the top upper edge of the polar coordinate image after transformation. Fewer pixels from the top upper edge are available for inclusion in the median filtering and limits the correction efficiency of the median filtering. Nevertheless, the dose distribution after ring artifact correction is consistent with the dose distribution of TPS.

Due to the unstable response of the optical detectors, ring artifacts appeared in the optical CT images acquired from PGDs and disturbed the following converted dose distributions. These artifacts cause circular fluctuation on the dose planes parallel to tomotherapy rotating ring and discontinuity on the dose planes perpendicular to the tomotherapy rotating ring. Eventually, these results lead to incorrect dose features and non-uniformity in the measured 3D dose distribution. To correct the ring artifacts in tomographic images, several methods based on sinogram processing (Münch et al., 2009; Tang et al., 2001) or image post-processing (Sijbers and Postnov, 2004; Prell et al., 2009) have been proposed. In the sinogram-processing method, ring artifacts, present as streak features in sinograms, are extracted using the wavelet or Fourier transform. Filtering or normalization is applied to the extract features to reduce the streak features, and ring artifact-reduced images can be reconstructed. In the post-processing method, images contaminated by the ring artifacts are transformed into polar coordinates to turn the artifacts as streak shape. Templates acquired from the uniform region of the images or median filtering are applied to reduce the ring artifacts. After inverse polar transformation, ring artifact-reduced images can be obtained. These methods show different advantages on the correction of ring artifacts. Different from common tomographic images, radiation dose distribution is usually continuous varied with fewer sharp features. In this study, the post-processing method of median filtering in the polar coordinate is used to reduce the ring artifacts in the dose distribution from optical CT readout. The implementation and adjustment of the method are simple. As shown in the results, the ring artifacts in the optical CT images were effectively reduced, and the continuity and uniformity of the converted dose distribution were improved.

4. Conclusions

In this study, we used the NIPAM PGDs and optical CT imaging to measure the 3D dose distribution of treatment performed by the HT. The results indicated that the PGDs could effectively record the dose distribution formed by the multiple beams of the HT. Also, ring artifact correction by median filtering along the radial direction of the polar coordinate system with an appropriate filter length could further improve the quality of the optical CT images and prevent artifact-resultant dose features appeared in the following converted dose maps. We concluded that the NIPAM PGDs and the optical CT imaging with ring artifact correction could be applied to conduct clinical dose verification of the HT, thereby contribute to safeguarding radiotherapy quality.

Declaration of competing interest

The authors have no relevant conflicts of interest to disclose.

Acknowledgment

The authors would like to thank Ministry of Science and Technology, Taiwan for financially supporting this research under Contract No. MOST 107-2218-E-468-004-.

Appendix A. Supplementary data

Supplementary data to this article can be found online at https://doi.org/10.1016/j.radphyschem.2019.108572.

References

Baxter, P., Jirasek, A., Hilts, M., 2007. X-ray CT dose in normoxic polyacrylamide gel dosimetry. Med. Phys. 34, 1934–1943.

Chen, Y.L., Hsieh, B.T., Chiang, C.M., Shih, C.T., Cheng, K.Y., Hsieh, L.L., 2014. Dose verification of a clinical intensity-modulated radiation therapy eye case by the magnetic resonance imaging of N-isopropylacrylamide gel dosimeters. Radiat. Phys. Chem. 104, 188–191.

Fiorino, C., Dell'Oca, I., Pierelli, A., Broggi, S., De Martin, E., Muzio, Di, Nadia, D.M., Longobardi, B., Fazio, F., Calandrino, R., 2006. Significant improvement in normal tissue sparing and target coverage for head and neck cancer by means of helical tomotherapy. Radiol. Oncol. 78 (3), 276–282.

Forrest, L.J., Mackie, T.R., Ruchala, K., Turek, M., Kapatoes, J., Jaradat, H., Hui, S., Balog, J., Vail, D.M., Mehta, M.P., 2004. The utility of megavoltage computed tomography images from a helical tomotherapy system for setup verification purposes. Int. J. Radiat. Oncol. Biol. Phys. 60 (5), 1639–1644.

Hsieh, L.L., Shieh, J.I., Wei, L.J., Wang, Y.Y., Cheng, K.Y., Shih, C.T., 2017. Polymer gel dosimeters for pretreatment radiotherapy verification using the three-dimensional gamma evaluation and pass rate maps. Phys. Med. 37, 75–81.

Johnston, H., Hilts, M., Jirasek, A., 2015. Incorporating multislice imaging into x-ray CT polymer gel dosimetry. Med. Phys. 42 (4), 1666–1677.

Krause, S., Beck, S., Schramm, O., Schubert, K., Hauswald, H., Bois, A.Z.D., Herfarth, K., Debus, J., Sterzing, F., 2013. Tomotherapy radiosurgery for arteriovenous malformations—current possibilities and future options with helical tomotherapy dynamic jaws? Technol. Cancer Res. Treat. 12 (5), 421–428.

Lee, T.F., Fang, F.M., Chao, P.J., Su, T.J., Wang, L.K., Leung, S.W., 2008. Dosimetric comparisons of helical tomotherapy and step-and-shoot intensity-modulated radiotherapy in nasopharyngeal carcinoma. Radiol. Oncol. 89 (1), 89–96.

Maryanski, M.J., Gore, J.C., Kennan, R.P., Schulz, R.J., 1993. NMR relaxation enhancement in gels polymerized and cross-linked by ionizing radiation: a new approach to 3D dosimetry by MRI. Magn. Reson. Imaging 11 (2), 253–258.

Münch, B., Trtik, P., Marone, F., Stampanoni, M., 2009. Stripe and ring artifact removal with combined wavelet-Fourier filtering. Opt. Express 17 (10), 8567–8591.

Oldham, M., Kim, L., 2004. Optical-CT gel-dosimetry II: optical artifacts and geometrical distortion. Med. Phys. 31 (5), 1093–1104.

Prell, D., Kyriakou, Y., Kalender, W.A., 2009. Comparison of ring artifact correction methods for flat-detector CT. Phys. Med. Biol. 54 (12), 3881.

Ramsey, C.R., Langen, K.M., Kupelian, P.A., Scaperoth, D.D., Meeks, S.L., Mahan, S.L., Seibert, R.M., 2006. A technique for adaptive image-guided helical tomotherapy for lung cancer. Int. J. Radiat. Oncol. Biol. Phys. 64 (4), 1237–1244.

Rochet, N., Sterzing, F., Jensen, A., Dinkel, J., Herfarth, K., Schubert, K., Eichbaum, M., Schneeweiss, A., Sohn, C., Debus, J., Harms, W., 2008. Strahlenther. Onkol. 184 (3), 145–149.

Senden, R.J., De Jean, P., McAuley, K.B., Schreiner, L.J., 2006. Polymer gel dosimeters with reduced toxicity: a preliminary investigation of the NMR and optical dose–response using different monomers. Phys. Med. Biol. 51 (14), 3301.

Shih, C.T., Hsu, J.T., Han, R.P., Hsieh, B.T., Chang, S.J., Wu, J., 2013. A novel method of estimating dose responses for polymer gels using texture analysis of scanning electron microscopy images. PLoS One 8 (7), e67281.

Shih, C.T., Chang, Y.J., Hsu, J.T., Chuang, K.S., Chang, S.J., Wu, J., 2015. Image reconstruction of optical computed tomography by using the algebraic reconstruction technique for dose readouts of polymer gel dosimeters. Phys. Med. 31 (8), 942–947.

Sijbers, J., Postnov, A., 2004. Reduction of ring artifacts in high resolution micro-CT reconstructions. Phys. Med. Biol. 49 (14), 247–253.

Stiebel-Kalish, H., Reich, E., Gal, L., Rappaport, Z.H., Nissim, O., Pfeffer, R., Spiegelmann, R., 2012. Visual outcome in meningiomas around anterior visual pathways treated with linear accelerator fractionated stereotactic radiotherapy. Int. J. Radiat. Oncol. Biol. Phys. 82 (2), 779–788.

Tang, X., Ning, R., Yu, R., Conover, D., 2001. Cone beam volume CT image artifacts caused by defective cells in x-ray flat panel imagers and the artifact removal using a wavelet-analysis-based algorithm. Med. Phys. 28 (5), 812–825.

Welsh, J.S., Patel, R.R., Ritter, M.A., Harari, P.M., Mackie, T.R., Mehta, M.P., 2002. Helical tomotherapy: an innovative technology and approach to radiation therapy. Technol. Cancer Res. Treat. 1 (4), 311–316.

Wendling, M., Zijp, L.J., McDermott, L.N., Smit, E.J., Sonke, J.J., Mijnheer, B.J., van Herk, M., 2007. A fast algorithm for gamma evaluation in 3D. Med. Phys. 34 (5), 1647–1654.

Wong, J.Y., Rosenthal, J., Liu, A., Schultheiss, T., Forman, S., Somlo, G., 2009. Image-guided total-marrow irradiation using helical tomotherapy in patients with multiple myeloma and acute leukemia undergoing hematopoietic cell transplantation. Int. J. Radiat. Oncol. Biol. Phys. 73 (1), 273–279.